JOURNAL OF PHYSICAL CHEMISTRY, 2025, Vol. 99, No. 1, c. 3–20

CHALLENGES, DEVELOPMENT TRENDS, AND CURRENT PROBLEMS OF PHYSICAL CHEMISTRY

MECHANISMS OF PRODUCTION AND DEATH OF SINGLET OXYGEN AND OZONE IN FAST-FLOW $O/O_2/N_2$ GAS MIXTURES

Yu. A. Mankelevich[a], *, T. V. Rakhimova[a], D. G. Voloshin[a], and A. A. Chukalovskii[a]

[a] *Lomonosov Moscow State University, D. V. Skobeltsyn Institute of Nuclear Physics, Moscow, Russia*

**e-mail: ymankelevich@mics.msu.su*

Received December 28, 2023
Revised July 11, 2024
Accepted July 15, 2024

Abstract. The experimental results of measurements of concentrations of $O_2(a^1\Delta_g)$ and $O_2(b^1\Sigma_g^+)$ in a fast-flow gas system with no plasma-chemical processes involving electrons and ions are described using a numerical spatially two-dimensional model. The dependences of $O_2(a^1\Delta_g)$ and $O_2(b^1\Sigma_g^+)$ concentration profiles on the gas pressure, the fraction of O atoms in O/N_2 mixtures, and O_2 additions to the gas mixture are obtained. The need to take into account the detailed vibrational kinetics of ozone and the processes of its formation on the tube surface in the model is shown. The treatment of the reaction of three-body recombination of O atoms on $M = N_2$, O_2 taking into account the reverse dissociation reaction of the formed highly excited molecule is proposed, and the functional dependence of the resulting coefficient $k_{rec}(T)$ — the rate of three-body recombination — is obtained, which agrees well with the measured temperature dependences $k_{rec}(T)$. The channels of further relaxation of the formed excited molecules and oxygen atoms are obtained.

Keywords: *singlet oxygen, recombination of oxygen atoms, vibrationally excited ozone, fast-flow gas system, two-dimensional modeling*

DOI: 10.31857/S00444537250101e3

1. INTRODUCTION

Chemical and plasma chemical kinetics in oxygen and its mixtures with nitrogen have long been and continue to be intensively studied in various fields, such as atmospheric chemistry [1–3], electric discharge plasma and its decay [4–9], barrier discharge-based ozone generators [10–15], laser photolysis of ozone and oxygen [3, 16–18], and kinetics of chemical conversions in fast-flow reactors [19, 20]. Despite the large number of publications and studies on these topics, some important aspects of oxygen chemical kinetics remain incompletely studied. For instance, the question of the mechanisms and primary products of the reaction of three-body oxygen recombination $O + O + M \rightarrow O_2^* + M$ ($M=O_2$, N_2), as well as the subsequent mixing and relaxation of the excited O_2^* products into the underlying electronic states of molecular oxygen remains open [21]. Such direct and stepwise relaxation processes in many systems can be important sources of singlet oxygen $O_2(a^1\Delta_g)$ and $O_2(b^1\Sigma_g^+)$.

In the cases of discharge plasmas, the rate of the relaxation processes of population of $O_2(a^1\Delta_g)$ and $O_2(b^1\Sigma_g^+)$ from the upper excited states of O_2 is usually much smaller than the rate of the electron impact excitation processes of $O_2(a^1\Delta_g)$ and $O_2(b^1\Sigma_g^+)$ from the $O_2(X^3\Sigma_g^-)$ ground state.

Therefore, experiments in fast-flow gas systems with recombining atomic oxygen in O/N_2 mixtures, rather than plasma systems, are more suitable for studying the process of three-body recombination and relaxation of its products. In addition, in a series of works by Ogryzlo et al. [19, 20], non-trivial dynamics of $O_2(a^1\Delta_g)$ and $O_2(b^1\Sigma_g^+)$ concentrations in various O/N_2 mixtures with and without admixing O_2 into the initial recombining gas flows were obtained in such systems. Thus, in these works, abrupt bursts of $O_2(a^1\Delta_g)$ and $O_2(b^1\Sigma_g^+)$ luminescence were observed for different pressures and gas mixtures immediately after the zone of admixing of different fractions of O_2 into the flow. An increase in singlet oxygen death in reactions with O_3 was expected due to additional ozone production in the reaction $O + O_2 + M \rightarrow O_3 + M$, i.e., the effect of O_2 additions opposite to the observed one. To date, publications lack a detailed description of the mechanisms of singlet oxygen production in the considered experiments, as well as a quantitative explanation of the obtained results, which requires at least two-dimensional 2-D(r,z)-modeling.

A series of experiments on long-wavelength (with the laser wavelength > 411 nm) photolysis of ozone [22]

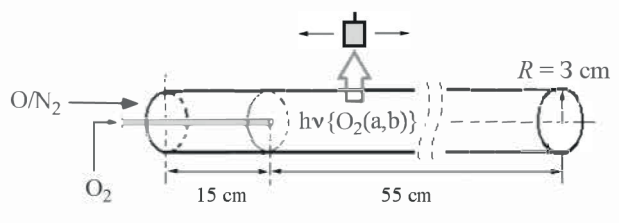

Fig. 1. Scheme of the fast-flow gas system.

indicated that in the reaction of O_3 with O there exists a channel with the products $O_2(a^1\Delta_g) + O_2$, the fraction of which does not exceed 20%. Recently, we performed simulations [23] of ozone laser photolysis experiments [16–18], where the dynamics of the $O_2(a^1\Delta_g)$ rapid decay was also measured. We developed a model of the vibrational kinetics of ozone molecules, which showed that ozone $O_3(v1,v2,v3)$ in various vibrational states, in addition to the known destruction of singlet oxygen in the reaction $O_2(a^1\Delta_g) + O_3(v) \rightarrow O + O_2 + O_2$, can also be its predominant source in the reactions $O_3(v1,v2,v3) + O \rightarrow O_2(a^1\Delta_g) + O_2$ under certain conditions. Thus, the results of the experiments [19, 20] allow verifying such a source of $O_2(a^1\Delta_g)$ introduced in the models in [23], as well as establishing the channel fraction of $O_2(b^1\Sigma_g^+)$ production in the reaction $O_3(v1,v2,v3) + O \rightarrow O_2(b^1\Sigma_g^+) + O_2$. A two-dimensional 2-D(*r,z*)-model adapted to the parameters and conditions of experiments in a fast flow reactor was used in this work to calculate the experiments [19, 20], taking into account the developed chemical kinetics from [23, 24]. Moreover, a new approach was tested in the kinetics model, which allows analytically calculating the temperature dependences of the rate coefficient of three-body recombination of O atoms observed in experiments. Section 2 of this work describes this approach and presents the kinetics of O/N mixtures, which determine the principal results of two-dimensional simulation of experiments in [19, 20]. Section 3 presents the results of calculations of axial and radial distributions of component concentrations and compares them with the experimental profiles of $O_2(a^1\Delta_g)$ and $O_2(b^1\Sigma_g^+)$ concentrations for different parameters and experimental conditions (tube pressure, fraction of O atoms in the mixture, and pressure of admixed O_2).

2. 2D MODEL OF PROCESSES IN FAST-FLOW $O/O_2/N_2$ GAS MIXTURES

2.1 2D(r,z)-Model and Schematic Diagram of a Fast-Flow Gas System

In this work, we perform 2D(*r,z*)-modeling of a fast-flow gas system in the main tube (70 cm long and 3 cm in radius), into which various specified fluxes of O atoms and N_2 molecules were delivered and along which measurements of singlet oxygen emission were performed. At a distance of 15 cm along the flow in the axial zone ($r = 0$), different flows of O_2 molecules were admixed. In the experiment, this was done through a thin tube moving along the axis, ending with a multiple-jet inlet. Figure 1 shows a simplified scheme of such a system used in our 2D modeling of the experiments of Ogryzlo et al. [19, 20].

There were no additional activation processes in the tube itself, and the tube walls were coated with halogen wax to reduce the probabilities of surface death of radicals, primarily O atoms (in [19], phosphoric acid was also used with the same results as for wax). In an additional thin tube with a radius of 0.5 cm, the N_2 stream was activated by the microwave discharge and then the NO stream was admixed into this partially dissociated nitrogen stream (N/N_2), achieving complete conversion of N atoms in the reaction $N + NO \rightarrow O + N_2$ and minimizing the residue of NO molecules. The O/N_2 flux thus obtained was injected from above into the beginning of the main tube, where the axial emission profiles of singlet oxygen were measured (Fig. 1).

The singlet oxygen emission measured along the tube, $O_2(a^1\Delta_g) \rightarrow O_2(X^3\Sigma_g^-) + h\nu$(1270 nm) [19] and $O_2(b^1\Sigma_g^+) \rightarrow O_2(X^3\Sigma_g^-) + h\nu$(762 nm) [20], were calibrated against a known source of NO_2^* emission. The details of the diagnostic systems, other parameters of the experimental setup, the modes studied and the results are described in detail in [19, 20]. Here, the experimental results for the modes used in the calculations will be presented in what follows along with the calculated distributions.

The developed 2D(*r,z*) two-dimensional model included the conservation equations for mass, momentums, and internal energy of the reaction gas mixture (taking into account components in the ground and excited states), equations of state, and thermochemical data of the components used. The model equations are described in detail in [25] for a cylindrical reactor with a hot filament and in [26] for a 2D(*r,z*)-model of a microwave discharge in a cylindrical resonator. These equations were solved numerically in cylindrical geometry until the steady-state mode was reached.

At the tube walls, the boundary conditions for the gas dynamic parameters were standard no-slip and impermeability conditions for the tangential and normal velocity components, respectively. At the inlet end of the tube, experimental flows of the injected O/N_2 mixture were set, with the free gas flow assumed

at the outlet end. In the cell (r = 0, z = 15 cm) corresponding to the O_2-gas input region, a local source $O_2(X)$ corresponding to the experimental flux $O_2(X)$ was set. The spreading of the concentration $O_2(X)$ from this source to the entire tube cross-section occurred a few centimeters downstream (at a length of ~5 cm downstream, z = 15–20 cm, the radial profile difference $(O_2(X))(r)$ was reduced to 50%, and a nearly uniform radial profile was reached at ~10 cm for z = 25 cm). The description of the experimental parameters was used to set gas flow rates corresponding to average gas flow velocities in the tube v_{av} ≈100 cm/s for the operating modes in $O_2(a^1\Delta_g)$ experiments [19] and 200 cm/s in $O_2(b^1\Sigma_g^+)$ experiments [20].

The chemical kinetics for the considered systems included more than 160 reactions for 16 components. The complete scheme of chemical kinetics in oxygen without taking into account the vibrationally excited ozone block is given in [24, 27] so here we discuss only some particular reactions of this scheme plus reactions involving N_2 molecules as a buffer component stable under the conditions involved. In [23], a kinetic scheme was developed for vibrationally excited ozone, including its ground state $O_3(0,0,0)$, the lower excited state $O_3(0,1,0)$ in the bending mode, $O_3(vc = 1)$ (combined lower states in the symmetric and antisymmetric modes $O_3(1,0,0) + O_3(0,0,1)$) and four effective states $O_3(vc)$ with the number vc of vibrational quanta $2 \leqslant vc \leqslant 5$. Taking into account the states with upper limit $vc = 5$ of the number of vibrational quanta is minimally required since such states are produced in the three-particle recombination $O + O_2 + M \rightarrow O_3(vc \leqslant 5) + M$. In the experiments involved, at pressures $\geqslant$ 1 Torr, rapid intramode mixing on O_2, N_2 molecules and O atoms ensure a near-equilibrium distribution within each effective state $O_3(vc \geqslant 2)$. This is dominated by the population of lower energy $O_3(0,vc,0)$ states with a fraction ~70% of the total population of the respective $O_3(vc)$ effective state at room temperature of the gas. In its turn, the exchange between the effective states occurs due to collisional V–T relaxation. The reaction scheme for vibrationally excited ozone is described in detail in [23, 28]. Here, in describing the reaction kinetics, we will limit ourselves to presenting only the key reactions that determine the balance of the components involved.

When setting the boundary conditions for the mixture components on the passivated tube surface, constant and sufficiently small probabilities of death were set so that there was no their appreciable influence on the calculated results. For the sake of certainty, all calculations were performed with the following probabilities of component death: $\gamma(O_2(a)) = 2 \times 10^{-5}$, $\gamma(O_2(b)) = 2\times10^{-4}$, $\gamma(O_2^{nt}) = 0.001$, $\gamma(O_2(h)) = 0.001$, $\gamma(O_3) = 10^{-6}$, $\gamma(O(^1D)) = 0.001$, $\gamma(O(^1S)) = 0.001$ (the component designations are explained below). For surface recombination of O atoms into molecular oxygen, a probability value of $\gamma(O) = 10^{-5}$ was used [29]. This death probability gave an order of magnitude smaller contribution to the total death of O atoms than gas-phase reactions. Moreover, the surface death of O atoms with ozone O_3 formed was also taken into account, and at large additions of molecular oxygen this additional death of atoms became dominant. It was taken into account in the framework of the developed mechanism of surface reactions of adsorption of O + S* => OadS on surface sites S* and the subsequent conversion to ozone $O_2(X)$ + OadS => $O_3(vc = 2,3)$ + S* [28] (under the conditions involved, this mechanism was the main source of ozone; it is discussed in detail below).

2.2 Three-Body Recombination Reaction of Oxygen Atoms

For the O/N_2 input mixtures, atomic oxygen is the only primary energy source for the formation and subsequent transformations of active particles, including singlet oxygen and ozone. Thus, three-body recombination of O atoms initiates the primary formation of electron and vibrational excitation of oxygen molecules.

We can assume that the primary weakly bound molecular products of three-body recombination

$$2O + M \leftrightarrow O_2^{nt} + M \qquad (1)$$

are the high electronic and vibrationally excited states of O_2^{nt} near the dissociation threshold, including, among others, the high (near-threshold) vibrationally excited levels of the Herzberg states (c1Σu−, Á3Δu, A3Σu+), the singlet oxygen states $O_2(b^1\Sigma_g^+)$ and $O_2(a^1\Delta_g)$, and the ground state $O_2(X^3\Sigma_g^-)$. Here, we consider O_2^{nt} as the effective (total) state of all O_2 near-threshold states without trying to deal with their partial contributions and complete composition, for instance, the inclusion of the $^5\Pi_g$ level studied in [21, 30]. Given the small difference $dE = E_{dis} - E_{nt}$ between the energies of these states $O_2^{nt} - E_{nt}$ and the dissociation threshold E_{dis}, these states will effectively decay during thermal dissociation (the reaction inverse to (1) and designated as (−1) in what follows) in the presence of active collisional processes (with the main gases M = N_2, O_2, O).

The competing fastest and most probable processes for the primary stabilization of O_2^{nt} should be those

associated with the relaxation of vibrational (*VT*) and rotational (*RT*) energy. For instance, sequential single-quantum (on M = N_2, O_2, and O) and multi-quantum (on M = O) vibrational relaxation [31] to more stable states ($c^1\Sigma_u^-$, $Á^3\Delta_u$, $A^3\Sigma_u^+$) (designated by O2(h) in what follows) with lower vibrational energy corresponding to lower vibrational states, for instance, v = 0–4. Moreover, various collisional and radiative transitions to lower electronic states (singlet $O_2(b^1\Sigma_g^+)$, $O_2(a^1\Delta_g)$, and ground state $O_2(X^3\Sigma_g^-)$ designated briefly by O_2(b), O_2(a), and O_2(X) in what follows) are also possible. It is the rate of all these transitions of O_2^{nt} to more stable states that will actually determine the recombination rate of O atoms

$$O_2^{nt} + M \Rightarrow O_2\,(\mathrm{h,b,a,X}) + M, M = N_2,\ O_2 \text{ and O}. \quad (2)$$

In the considered conditions of predominance of collisional processes, we neglected the radiative decay processes $O_2^{n\ t}$ => O2(h,b,a,X) + $h\nu$. The concentration of near-threshold states (considered as one effective O_2^{nt} state) is determined by the balance of processes (1), (–1), and (2), and its stationary value can be written as

$$\left[O_2{}^{nt}\right] = k_1 \times [O]^2 \Big/ (k_{-1} + k_2).$$

Here, in the general case of different rate coefficients of reactions (1),(2) on O_2 and N_2, the total coefficients written as

$$k_1 = \left(k_1{}^{O} \times [O] + k_1{}^{O2} \times [O_2] + k_1{}^{N2} \times [N_2]\right) \Big/ [M],$$
$$k_{-1} = \left(k_{-1}{}^{O} \times [O] + k_{-1}{}^{O2} \times [O_2] + k_{-1}{}^{N2} \times [N_2]\right) \Big/ [M],$$
$$k_2 = \left(k_2{}^{O} \times [O] + k_2{}^{O2} \times [O_2] + k_2{}^{N2} \times [N_2]\right) \Big/ [M]$$

for the total concentration $[M]=[N_2]+[O_2]+[O]$ are used.

The rate $R_2=k_2\times[O_2{}^{nt}][M]$ of collisional relaxation of O_2^{nt} to all underlying O_2 states will determine the resulting rate coefficient of three-body recombination of O atoms

$$k_{rec} = R_2 \Big/ \left([O]^2 [M]\right) = k_1 \times k_2 / (k_{-1} + k_2).$$

It follows from this treatment of recombination that it is the coefficient $k_{rec}(T)$, rather than $k_1(T)$ that is experimentally measured (for instance, by the dynamics of the leaving O atoms for different gas temperatures T). One can expect that against the background of exothermic barrier-free reactions (1) and (2), the temperature dependence $k_{rec}(T)$ will be determined mainly by the dependence $k_{-1}(T)$ of the endothermic reaction coefficient (–1). Under the assumption of the Arrhenius dependence $k_{-1}(T)=k0_{-1}(s) \times \exp(-E(s)/T)$, we have some scattering of the reaction barriers E(s) for the high vibrationally excited states of different $O_2(s,v\sim v_{max})$, s = h,b,a,X. A characteristic estimate of E(s) can be the vibrational quanta of these states for the limiting vibrational levels $v\sim v_{max}$ at the dissociation threshold. Typical values of such quanta according to NIST [32] lie in the range $E(s) = 950 \pm 400$ K: E(s)~550 K for O_2(h), ~980 K for O_2(b) and O_2(a), ~1350 K for O_2(X). For constant coefficients k_1, k_2, pre-exponent $k0_{-1}$, and one characteristic barrier E_{nt}, the temperature dependence $k_{rec}(T)$ takes the following functional form

$$k_{rec}(T) = k_1 \Big/ \left(1 + \left(k0_{-1}/k_2\right) \times \exp\left(-E_{nt}/T\right)\right).$$

In publications, for M = N_2 there are results of measurements of $k_{rec}(T)$ for different temperatures, for instance, T = 196 K [33] and T = 298 K [33, 34]. And for room temperature, there is a scatter of results from $k_{rec}(T = 298\ \mathrm{K}) \approx 3 \times 10^{-33}$ (accepted in works on combustion) to 5×10^{-33} cm^6/s (used in atmospheric chemistry models) [34]. Here, we normalized to the results of [33] with an approximation of the temperature dependence $(4.7 \pm 0.4) \times 10^{-33} \times (300/T)^2$ [21]. For M = O_2, approximately similar values of the coefficient k_{rec} have been reported [32]. This dependence can be approximated by the formula for $k_{rec}(T)$ with E_{nt} = 600 K, ratio $(k0_{-1}/k_2)$ = 61, and $k_1 = 4.6 \times 10^{-32}$ cm^6/s, as can be seen in Fig. 2. Note that the previous sharper dependence in the experiments [29] in the range T = 196–330 K is almost perfectly approximated by the formula for $k_{rec}(T)$ with E_{nt} = 900 K, ratio $(k0_{-1}/k_2)$ = 165 and $k_1 = 2.85 \times 10^{-32}$ cm^6/s (Fig. 2). Since the coefficients $k0_{-1}$ and k_2 are included in the formula for $k_{rec}(T)$ as a ratio, their absolute values cannot be established from the results of $k_{rec}(T)$ measurements. These coefficients were determined in this work within the framework of the presented reaction kinetics of oxygen component production and death, which allows us to describe the axial O_2(a) and O_2(b) profiles in different experimental modes from [19, 20]. The developed kinetics (Table 1) and the obtained values $k0_{-1} = 2.15 \times 10^{-11}$ and $k_2 = 3.5 \times 10^{-13}$ cm^3/s are discussed in the subsequent sections.

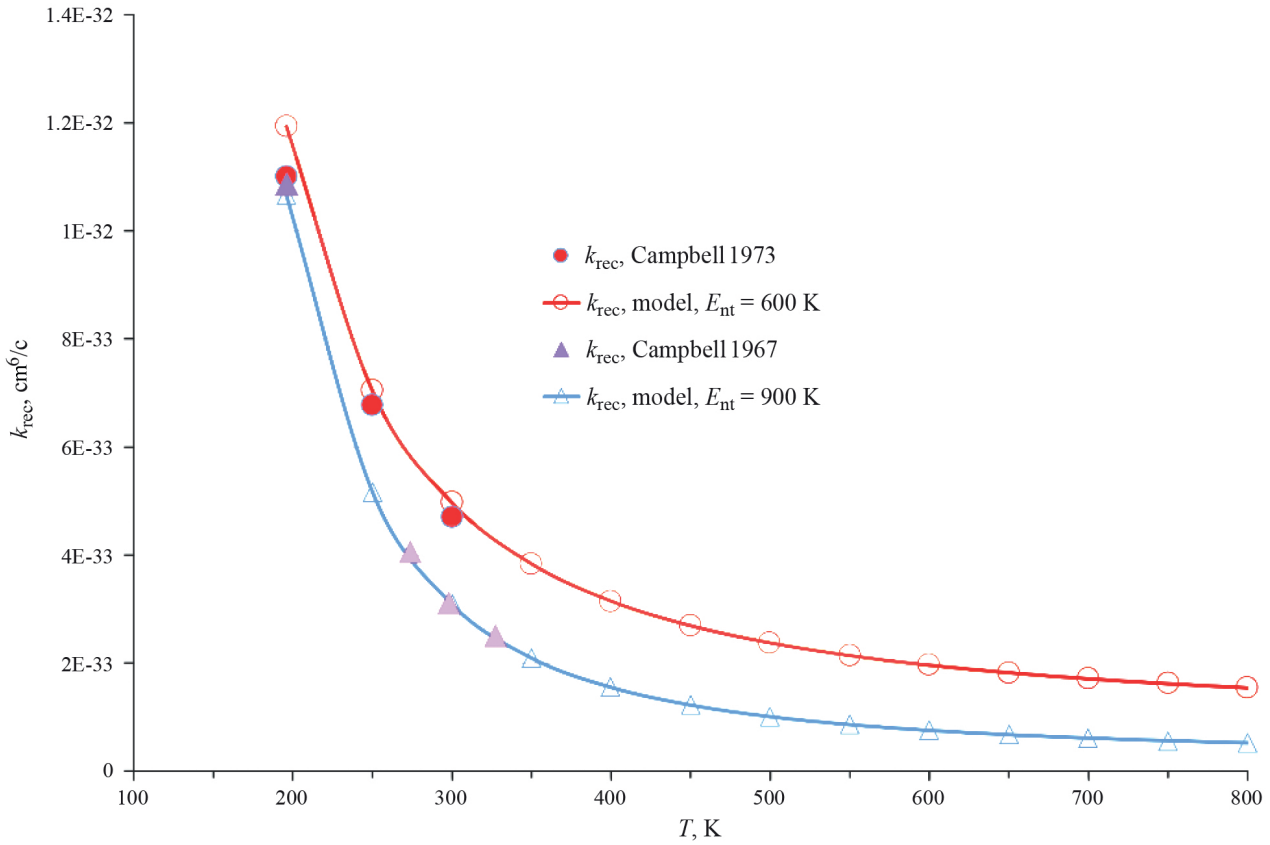

Fig. 2. Three-body recombination coefficient on M = N_2 depending on the gas temperature in the model and experiment according to data from [33] and [29].

2.3 Chemical Kinetics in a Recombining $O/O_2/N_2$ Mixture

The previous section gives an idea of the interrelation of the processes of atomic recombination and relaxation of excited oxygen molecules. This system cannot be described within the framework of complete level-by-level kinetics due to the many unknown processes with vibrationally and electronically excited O_2 molecules. For the purposes of this work, the necessary details of the key relaxation and reaction processes have been developed. For this purpose, all possible channels of O_2^{nt} relaxation to the underlying states $O_2(s)$, s = h,b,a,X and $O_2(h)$ relaxation to $O_2(s)$, s = b,a,X were included in the reaction scheme, followed by a variation of the rate coefficients of these processes.

For 2D calculations, the basic chemical kinetics of neutral components developed in previous works [23, 24, 28] was modified and extended. In addition to modifying the above described treatment of the reaction of three-body recombination of O atoms, the O_2^{nt}, $O_2(h)$ quenching reactions, the $O_3(vc) + O \rightarrow O_2(b) + O_2(X)$ reaction channel (much smaller than the main channels with the products $O_2(a) + O_2(X)$ (25%) and $2O_2(X)$ (75%) [23, 28]) were added/modified. The quenching of O_2^{nt} on M=N_2, O_2, and O was assumed to proceed mainly in $O_2(h)$ [35]. In turn, the quenching of these $O_2(h)$ states was an important source of $O_2(a)$ and $O_2(b)$. Such channels have been studied in detail in [30], where it is shown that the quenching of $O_2(h)$ on $O_2(X)$ results in a possible channel with the products $O_2(a) + O_2(b)$. Reaction (4a) of similar type $O_2(h) + O_2(a) \rightarrow O_2(b) + O_2(a)$ was added to the scheme, but its contribution to the production of $O_2(b)$ was negligible.

The possibility of the reaction $O_2^{nt} + O_2(a) \rightarrow$ $\rightarrow O_2(b)$ + product as a source of $O_2(b)$ also cannot be ruled out either. However, its efficiency would require an extremely large rate coefficient $>3 \times 10^{-10}$ cm^3/s, so this reaction is not included in the process scheme in this work. Exothermic reactions (6a), (b) of $O_2(h)$ c ozone were added as possible sources of $O_2(a)$ and $O_2(b)$. Such a source for $O_2(a)$ was introduced in [36] with an extremely high constant of 2×10^{-10} cm^3/s, 20 times higher than that used in this work. These additional sources for $O_2(a)$ and $O_2(b)$ provide good agreement with the experimental profiles and trends for all modes considered.

Table 1. Developed kinetic scheme of the production and death reactions of oxygen components (O, O_2(a), O_2(b), O_2(h), O_2^{nt}, O_3(*vc*)) in recombining $O/O_2/N_2$ mixtures. The reaction coefficients are presented as $k = k0 \times T^q \times \exp(-E/T)$; here, the values of E and T are in Kelvin degrees (K), and the coefficients k of two- and three-body reactions are in cm^3/s and cm^6/s, respectively.

N	Reactions	*k*0	*q*	*E*	References
(1)	$O + O + M \rightarrow O_2^{nt} + M$	4.6E-32	0.	0.	this work
(−1)	$O_2^{nt} + M \rightarrow O + O + M$	2.15E-11	0.	600.	
(2a)	$O_2^{nt} + N_2 \rightarrow O_2(h) + N_2$	3.35E-13	0	0	this work
(2b)	$O_2^{nt} + N_2 \rightarrow O_2(b) + N_2$	1.0E-17	0	0	this work
(2c)	$O_2^{nt} + N_2 \rightarrow O_2(a) + N_2$	1.4E-15	0	0	this work
(2d)	$O_2^{nt} + N_2 \rightarrow O_2 + N_2$	1.1E-14	0	0	this work
(2e)	$O_2^{nt} + O_2 \rightarrow O_2(h) + O_2$	1.42E-13	0	0	this work
(2f)	$O_2^{nt} + O_2 \rightarrow O_2(b) + O_2(a)$	3.7E-15	0	0	this work
(2g)	$O_2^{nt} + O_2 \rightarrow O_2(a) + O_2$	1.8E-13	0	0	this work
(2h)	$O_2^{nt} + O_2 \rightarrow O_2 + O_2$	2.3E-14	0	0	this work
(2i)	$O_2^{nt} + O \rightarrow O_2(h) + O$	1.E-11	0	0	this work
(2j)	$O_2^{nt} + O \rightarrow O_2 + O(^1S)$	4.5E-11	0	0	[38]
(3a)	$O_2(h) + N_2 \rightarrow O_2(b) + N_2$	1.0E-17	0	0	this work
(3b)	$O_2(h) + N_2 \rightarrow O_2(a) + N_2$	1.4E-15	0	0	this work
(3c)	$O_2(h) + N_2 \rightarrow O_2 + N_2$	1.1E-14	0	0	this work
(4a)	$O_2(h) + O_2 \rightarrow O_2(b) + O_2(a)$	3.7E-17	0	0	this work
(4b)	$O_2(h) + O_2 \rightarrow O_2(a) + O_2$	1.8E-13	0	0	[39]
(4c)	$O_2(h) + O_2 \rightarrow O_2 + O_2$	2.3E-14	0	0	[39]
(5a)	$O_2(h) + O \rightarrow O_2 + O$	5.E-13	0	0	this work
(5b)	$O_2(h) + O \rightarrow O_2 + O(^1S)$	1.E-14	0	0	this work
(6a)	$O_2(h) + O_3 \rightarrow O + O_2(b) + O_2$	1.5E-12	0.	0.	this work
(6b)	$O_2(h) + O_3 \rightarrow O + O_2(a) + O_2$	1.E-11	0.	0.	this work
(7)	$O(^1S) + N_2 \rightarrow O(^1D) + N_2$	5.E-17	0	0	[40]
(8a)	$O(^1S) + O_2 \rightarrow O(^1D) + O_2$	1.2E-12	0	850	[41]
(8b)	$O(^1S) + O_2 \rightarrow O(^3P) + O_2(a)$	2.2E-12	0	850	this work
(9)	$O(^1S) + O_2(a) \rightarrow O(^1D) + O_2(b)$	1.5E-10	0	0	this work
(10)	$O(^1S) + O \rightarrow O(^1D) + O$	3.5E-11	0	307	[42]
(11)	$O(^1S) + O_3 \rightarrow O(^1D) + O + O_2$	5.8E-10	0.	0.	[43]
(12)	$O(^1D) + N_2 \rightarrow O(^3P) + N_2$	2.1E-11	0	−115	[44]
(13a)	$O(^1D) + O_2 \rightarrow O(^3P) + O_2$	6.0E-12	0	−67	[45]
(13b)	$O(^1D) + O_2 \rightarrow O(^3P) + O_2(b)$	2.6E-11	0	−67	[45]
(14)	$O(^1D) + O(^3P) \rightarrow O(^3P) + O(^3P)$	8.0E-12	0	0	[46]
(15)	$O(^1D) + O_3 \rightarrow O + O + O_2$	2.37E-10	0.	0.	[44]
(16)	$O_2(b) + N_2 \rightarrow O_2(a) + N_2$	8.0E-20	1.5	−503.	[36]
(17)	$O_2(b) + O_2 \rightarrow O_2(a) + O_2$	7.4E-17	0.5	1104.7	[36]
(18a)	$O_2(b) + O \rightarrow O_2(a) + O$	7.E-14	0	0	[47]
(18b)	$O_2(b) + O \rightarrow O_2 + O$	1.E-14	0.	0.	[47]
(19a)	$O_2(b) + O_3 \rightarrow O + O_2 + O_2$	1.5E-11	0.	0.	[47]
(19b)	$O_2(b) + O_3 \rightarrow O_2 + O_3(vc = 5)$	7.0E-12	0.	0.	[47]
(20)	$O_2(a) + N_2 \rightarrow O_2 + N_2$	6.3E-22	0.8	0	[37]
(21)	$O_2(a) + O_2 \rightarrow O_2 + O_2$	1.26E-20	0.8	0	[48]
(22)	$O_2(a) + O \rightarrow O_2 + O$	1.3E-16	0	0	[49]
(23)	$O_2(a) + O_3 \rightarrow O + O_2 + O_2$	5.2e-11	0	E23i	[50]

Table 1. (End)

N	Reactions	$k0$	q	E	References
(24a)	$O + O_2 + N_2 \rightarrow O_3(vc = 1) + N_2$	1.23E-27	−2.8	0.	[23]
(24b)	$O + O_2 + N_2 \rightarrow O_3(vc = 2) + N_2$	1.76E-27	−2.8	0.	[23]
(24c)	$O + O_2 + N_2 \rightarrow O_3(vc = 3) + N_2$	1.05E-27	−2.8	0.	[23]
(24d)	$O + O_2 + N_2 \rightarrow O_3(vc = 4) + N_2$	5.27E-28	−2.8	0.	[23]
(24e)	$O + O_2 + N_2 \rightarrow O_3(vc = 5) + N_2$	3.51E-28	−2.8	0.	[23]
(25a)	$O + O_2 + O_2 \rightarrow O_3(vc = 1) + O_2$	1.4E-29	−2.	0.	[23]
(25b)	$O + O_2 + O_2 \rightarrow O_3(vc = 2) + O_2$	2.0E-29	−2.	0.	[23]
(25c)	$O + O_2 + O_2 \rightarrow O_3(vc = 3) + O_2$	1.2E-29	−2.	0.	[23]
(25d)	$O + O_2 + O_2 \rightarrow O_3(vc = 4) + O_2$	0.6E-29	−2.	0.	[23]
(25e)	$O + O_2 + O_2 \rightarrow O_3(vc = 5) + O_2$	0.4E-29	−2.	0.	[23]
(26a)	$O + O_3 \rightarrow O_2 + O_2$	6.E-12	0.	E26i	[23]
(26b)	$O + O_3 \rightarrow O_2(a) + O_2$	2.E-12	0.	E26i	[23]
(26c)	$O + O_3 \rightarrow O_2(b) + O_2$	1.E-13	0.	E26i	this work

Rate coefficients and multiple channels for reactions involving electronically excited oxygen molecules (and even more so for those involving two excited reactants) have been established in publications with great uncertainty. In this work, we tested different sets of reaction constants for the principal modes (for which the spatial profiles of $O_2(a)$ and $O_2(b)$ concentrations are given) and a number of additional modes from [19, 20]. As a result, a kinetic scheme (given in Table 1) was developed that provides a quantitative and qualitative description of the experimental profiles of $[O_2(a)](z)$ and $[O_2(b)](z)$ concentrations and their dependences on the mole fractions of O and $O_2(X)$ in the main gas N_2, and on the pressure of the gas mixture. Table 1 gives the rate coefficients $k_i = k0_i \times T_b \times \exp(-E_i/T)$ in cm^3/s for two-body reactions and in cm^6/s for three-body reactions, T is the gas temperature, and E_i are the activation energies in [K]. The last column of Table 1 contains references to works where the coefficients of the respective reactions were studied or used. The reference "this work" corresponds to the coefficients obtained and used in this work. In reactions (1), (2), the third body is $M = N_2$, O_2, and O. In the reactions, the designations O, O_2, and O_3 correspond to $O(^3P)$, $O_2(X)$, and all ozone states, $O_3(000)$, $O_3(010)$ and the effective vibrational states $O_3(vc = 1–5)$. For reaction (20), $k_{20} < 6.7e–20$ cm^3/s in [37]. For reaction (23), $E23_i = 2840$, 1900, 1700, 1300, 0, 0, 0 K for $O_3(000)$, $O_3(010)$, $O_3(vc = 1–5)$. For reaction (26), $E26_i = 2060$, 1400, 1200, 900, 0, 0, 0 K for $O_3(000)$, $O_3(010)$, $O_3(vc = 1–5)$.

The identified key processes and the spatial variations of their rates are discussed in detail below in Sections 3 and 4, together with the calculated spatial distributions of the concentrations of components of the $O/O_2/N_2$ mixtures.

The admissible limits for the O_2^{nt} and $O_2(h)$ relaxation rate coefficients were established using 2D(r,z)-model calculations of the simplest modes for an O/N_2 mixture (without $O_2(X)$ added) with a minimum number of significant reactions. 2D calculations with different sets of reaction coefficients were then performed for different $O_2(X)$ additions, to analyze key processes and the necessary correlation with experimental profiles along the tube of $O_2(a)$ and $O_2(b)$ concentrations [19, 20]. These profiles show complex dependences on the added fraction of $O_2(X)$ in the O/N_2 mixture (these profiles are given in Sections 3 and 4).

2.4 Kinetics of Reactions of Ozone formation on the Surface

Coating the tube walls of the fast-flow reactor with passivating compositions was done to minimize the role of surface processes in the balance of production and death of the mixture components. However, the exact level of drop in probabilities of surface death of components is not known. In addition, surface poisoning may occur during the process, which may lead to an increase in the probability of death [51]. The occurrence of additional processes with active oxygen particles on such surfaces or the intensification of individual processes at different wax surface sites cannot be excluded.

The model in this work includes the surface mechanism of ozone formation found in [28] on pyrex tube walls. This mechanism includes the reactions

$$O + O_{ad}S \rightarrow O_2 + S^*, \quad \text{(s1)}$$

$$O + S^* \rightarrow O_{ad}S, \quad \text{(s2)}$$

$$O_2 + O_{ad}S \rightarrow O_3(vc) + S^*, \quad \text{(s3)}$$

where (s1) is recombination of the incident and adsorbed O atoms, (s2) is adsorption of the O atom on the surface site S*, (s3) is recombination into ozone by the incident $O_2(X)$ molecule with the adsorbed O atom. For the alternate tube wall surface considered here, the parameters of this reaction mechanism were modified.

In [28], it was found that adsorbed O atoms ($O_{ad}S$) with adsorption energies of 0.6–1 eV recombine with the incident $O_2(X)$ molecules to form vibrationally excited $O_3(vc \leqslant 3)$ ozone. The ozone source FS_{O3} [$cm^{-2}s^{-1}$] can be analytically expressed by the following function of [O_2], [O] concentrations at the wall and two parameters $a = k_{s2}[S_0]$ and $b = k_{s3}/(k_{s1} + k_{s2})$

$$FS_{O3} = ab[O_2]/(1 + b[O_2]/[O]). \quad \text{(s4)}$$

Here, k_{s1}, k_{s2}, and k_{s3} are the coefficients (in cm^3s^{-1}) of reaction rates (s1,s2,s3), $S_0 = [S^*] + [O_{ad}S]$ is the total concentration (in cm^{-2}) of surface sites providing the mechanism (s1)–(s3). The parameters a and b were varied, with the most acceptable approximations of the axial profiles of $O_2(a)$ and $O_2(b)$ achieved for $a = 31.7$, $b = 0.003$ and the distribution $20\%O_3(vc = 3)/80\%O_3(vc = 2)$ of recombination products of reaction (s3).

This surface FS_{O3} ozone source ensures the dominant part of ozone production compared to its gas-phase production in the three-body recombination of $O + O_2 + M$. Without this source of vibrationally excited ozone, the resulting calculated $O_2(a)$ and $O_2(b)$ profiles differ significantly from the experimental profiles. This source also leads to a significant (especially at large $O_2(X)$ additions) increase in the additional FL_O death of O atoms.

The vibrational and reaction kinetics of ozone are discussed in detail in [28] in the afterglow of a DC discharge and in [23] under the conditions of various photolytic experiments.

3. PRODUCTION/DEATH AND SPATIAL DISTRIBUTIONS OF $O_2(a)$ IN A FAST-FLOW GAS SYSTEM IN $O/O_2/N_2$-MIXTURES

2D(r,z)-model calculations with the developed kinetics (Table 1) of three modes with different $O_2(X)$ additions to the inlet flow of $0.11\%O/N_2$ mixture (the gas pressure is $p_{gas} = 6$ Torr) showed good agreement with the profiles measured [19] along the tube of the diameter-averaged $O_2(a)$ concentrations (Fig. 3).

As one can see from Fig. 3, when there are no $O_2(X)$ additives, the $O_2(a)](z)$ concentration grows almost linearly along the flow along the z-axis, which implies that the local sources of singlet oxygen are approximately constant along the flow (constant difference in the rates of its production and death). Here, a slight decrease in the gradient of the $[O_2(a)](z)$ profile for $z < 30$ cm is observed in the computational and experimental results, but it is more pronounced in the latter, possibly due to the difference between the model and experimental geometry of the O/N_2 gas injection system. When $O_2(X)$ is introduced into the flow in the axial region of the tube at the point $z \sim 15$ cm, a drastic increase in both $[O_2(a)](z > 15$ cm) and $[O_2(b)](z > 15$ cm) is observed, indicating the inclusion of additional singlet oxygen production processes. Moreover, as the $O_2(X)$ fraction is further increased, the $[O_2(a)](z)$ and $[O_2(b)](z)$ are observed to reach saturation and then even drop at $O_2(X)$ partial pressure $p_{O2} > 0.04 \times p_{gas}$, where p_{gas} is the total gas pressure in the tube. This means that there is inclusion of singlet oxygen destruction processes associated with the emerging derivative oxygen components (such as ozone). The influence of only the different quenching efficiencies of O_2^{nt} and $O_2(h)$ on $M = O_2(X)$ as compared to $M = N_2$ alone cannot reproduce these non-monotonic $[O_2(a)](z)$ and $[O_2(b)](z)$ profiles. At the same time, the addition of recently developed ozone kinetics including relaxation, reactions, and surface sources of vibrationally excited ozone [23, 28] to the kinetic scheme showed, under the experimental conditions involved, the importance of reactions with ozone for both singlet oxygen death and production.

The profiles shown in Fig. 3 are established as a result of the total balance of $O_2(a)$ production and death reactions illustrated in Fig. 4 for oxygen addition $p_{O2} = 0.25$ Torr. We consider the roles of the principal reactions in establishing the $O_2(a)$ profiles and discuss the dependencies of $O_2(a)$ on the gas pressure and the fraction of O atoms in the original mixture.

We begin with the simplest case with no $O_2(X)$ additive. For it, as we can see from the reaction rates in the unperturbed zone $z < 10$ cm (Fig. 4), the $O_2(a)$ production is determined only by the reaction rate $R3b = k3b[O_2(h)][N_2]$

$$O_2(h) + N_2 \rightarrow O_2(a) + N_2, \quad \text{(3b)}$$

exceeding the other reactions of $O_2(a)$ production and death by an order of magnitude or more. This is the imbalance that persists for the entire tube in the simplest mode with no $O_2(X)$ additive when a nearly

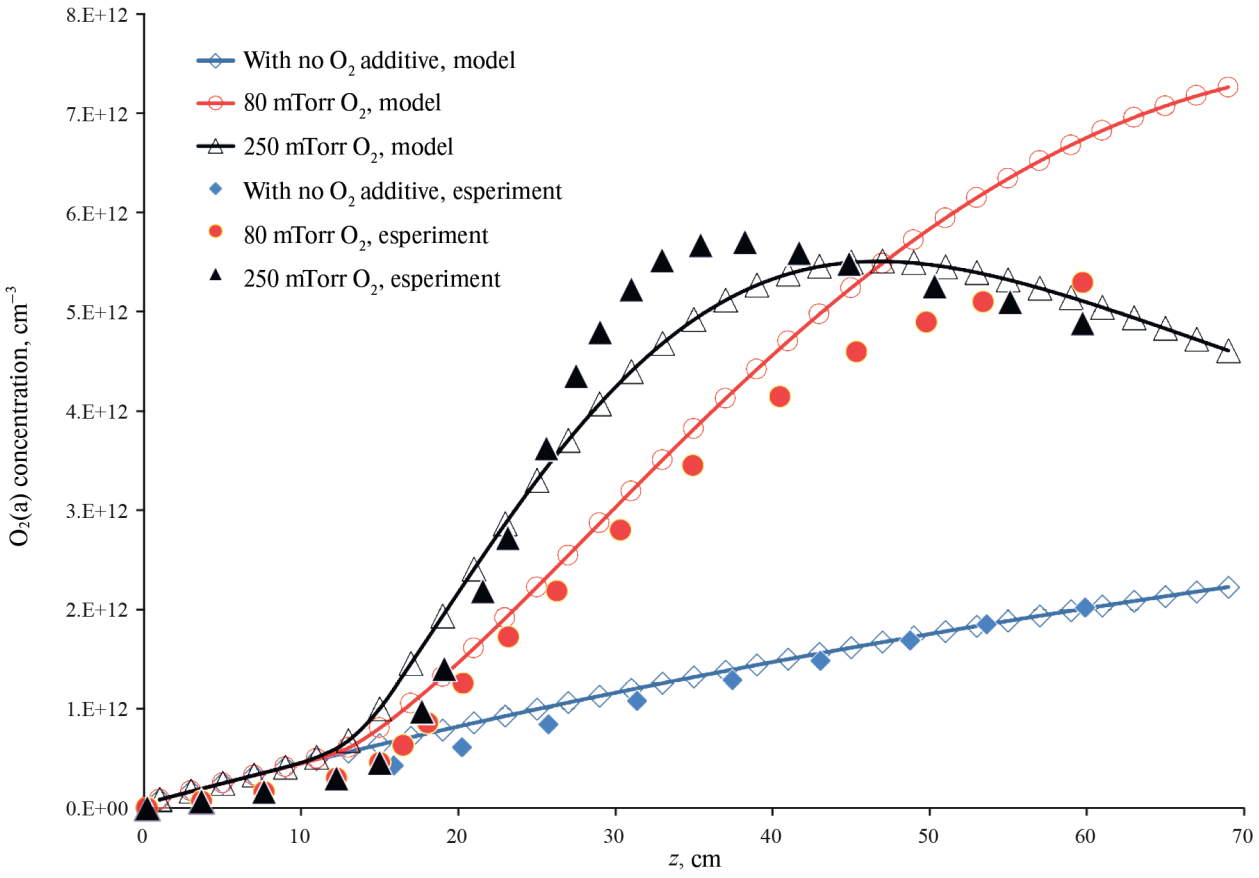

Fig. 3. Axial distributions of the tube diameter-averaged $O_2(a)$ concentrations in the 2D model and experiment [19] for different $O_2(X)$ additions (in the axial region of the tube at z~15 cm) to the inlet flow of 0.11%O/N_2 mixture, the gas pressure in the tube is p_{gas} = 6 Torr.

linear growth of $[O_2(a)]$ is observed (Fig. 3, curve and points "with no O_2 additive"). In this mode, the quasi-stationary concentrations of $[O_2(h)]$ and $[O_2^{nt}]$ are established as a result of the balance of principal reactions (2a), (3), (5), and (1), (–1), respectively,

$$\left[O_2(h)\right] \approx k_{2a}\left[O_2^{nt}\right][N_2]/\left(k_3[N_2] + k_5[O]\right),$$
$$\left[O_2^{nt}\right] \approx k_1[O]^2/k_{-1}.$$

In this case, the $O_2(a)$ production will have the following functional dependence on [O] and $[N_2]$: $R3b \sim A[O]^2[N_2]$, where $A = k_{3b}k_{2a}k_1(k_{-1}(k_3 + k_5[O][N_2]))$. In the case $k_3 >> k_5[O]/[N_2]$, the $R3b$ production will be close to the second order with respect to the [O] concentration ($R_{3b} \sim [O]^m$, m~2) and to the first order with respect to $[N_2]$ (i.e., actually with respect to the pressure p_{gas}). Roughly such orders were obtained both in the experiments [19], where m = 1.9, and in our computational results, where m = 1.9 was achieved for the reaction coefficient ratio $k_3/k_5 \sim 0.03$ in the developed scheme with $k_3 = k_{3a} + k_{3b} + k_{3c} \approx 1.5 \times 10^{-14}$ and $k_5 = 5 \times 10^{-13}$ cm^3/s.

Note the scatter of used values of k_5 in publications, from $k_5 = 5 \times 10^{-14}$ in [52, 53] to $k_5 = 1.3 \times 10^{-11}$ in [36]. The coefficient $k_{3b} = 1.4 \times 10^{-15}$ cm^3/s of reaction (3b) was set from the condition of the closest approximation to the experimental almost linearly growing profile $[O_2(a)]_{av}(z)$ (Fig. 3). For similar reaction (2c) ($O_2^{nt} + N_2$), the same constant $k_{2c} = k_{3b}$ was used. The full constant k_3 was determined during the calculations of modes with $O_2(X)$ additives and depended on the constant of reaction (4b) $O_2(h) + O_2 => O_2(a) + O_2$ [39].

As one can see from Fig. 3, the $O_2(a)$ profile changes dramatically with $O_2(X)$ additives in the region of $O_2(X)$ injection and downstream of the gas flow. As it was found in [19], the order of dependence of the $O_2(a)$ production rate on [O] immediately beyond the $O_2(X)$ injection zone decreases down to first order for large $O_2(X)$ additives. Calculations show that in the $O_2(X)$ injection zone and further downstream, $O_2(a)$ production still significantly exceeds $O_2(a)$ death.

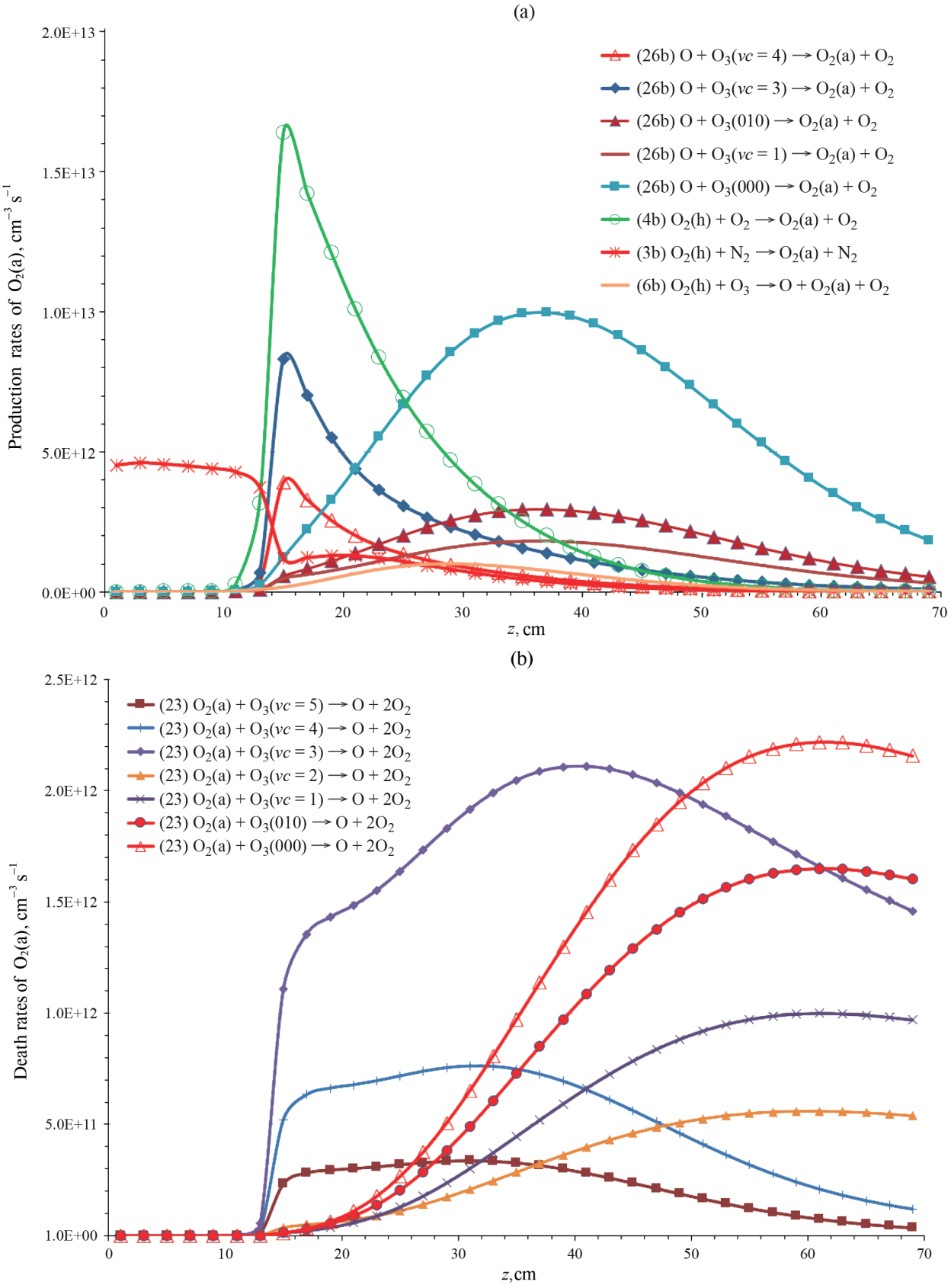

Fig. 4. Axial (z,r = 0.75) distributions of production (a) and death (b) rates of O_2(a) for the mode with 0.25 Torr O_2(X) added to the inlet flow of the 0.11%O/N_2 mixture, the gas pressure in the tube is p_{gas} = 6 Torr.

As $O_2(X)$ additive increases, this production begins to be driven by reactions of O atoms with ozone, and reaction (4b) of $O_2(h)$ with $O_2(X)$ (Fig. 4a). Reaction (4b) leads to a growing drop in $[O_2(h)](z \geqslant 15$ cm) concentration by a factor of two or more for large $O_2(X)$ additives (Fig. 5). Moreover, in and beyond the $O_2(X)$ injection zone ($z \geqslant 15$ cm), O death in reactions (26a), (26b), and (26c) with O_3 (predominantly with vibrationally excited ozone) also begins to progressively lower the $[O](z \geqslant 15$ cm) concentration as compared to the initial concentration at $z = 0$ (Fig. 5). This drop of [O] when $z \geqslant 15$ cm mainly determines the apparent and detected in the experiment [19] lowering of the order of the $[O_2(a)] \sim [O]^m$ dependence. According to the technique of determining the order m in the experiment without taking into account the [O] drop when $z > 15$ cm, a drop of m similar to the experimental one can also be obtained in the calculations. To conclude this analysis, we note the effect on the $[O_2(a)]_{av}(z \geqslant 15$ cm) profiles of reaction (4b) [39] (where this channel was assumed to be the main channel for the quenching of $O_2(h)$ by $O_2(X)$ molecules) and introduced reaction (6b) ($O_2(h) + O_3$). If we remove these reactions from the scheme, the agreement between the calculated and experimental $O_2(a)$ profiles deteriorates for big $O_2(X)$ additives: for $p_{O2} = 0.25$ Torr, the maximum $[O_2(a)]_{av}$ in Fig. 3 will shift to the right ~2 cm further away from the experimental maximum and drop by ~15%.

The main fraction of ozone under the considered conditions is produced as a result of surface reactions (s2), (s3) [23, 28], rather than in the gas phase as a result of three-body reactions (24), (25) $O + O_2(X) + M \rightarrow$ $\rightarrow O_3(vc) + M$. The *VT* relaxation reactions of ozone to N_2, O_2, and O tend to smooth out the non-equilibrium ozone production in gas-phase and surface reactions [28], but fully quasi-equilibrium distributions over the vibrational states of ozone are not established even at the end of the tube. The total ozone concentration increases rather drastically along the tube downstream (Fig. 5) due to surface source (s3), which is simultaneously an important dearth for O atoms. This death, in conjunction with the death of odd oxygen in reaction (26) of O with ozone, leads to a significant drop in [O] concentration at the end of the tube for large $O_2(X)$ additives (Fig. 5). For large $O_2(X)$ additives, this drop in [O] leads to a curvature of the $[O_2(a)](z)$ profile, as one can see in Fig. 3 for the case of maximum additive $p_{O2} = 0.25$ Torr. Special calculations without a surface ozone source did not give any bending of the $[O_2(a)]$ (z) profile for this $O_2(X)$ additive; on the contrary, it remained growing along the entire length of the tube. A picture similar to Fig. 4 of the rate of $O_2(a)$ production and death processes is also observed for lower $O_2(X)$ additions only with a lower ozone production rate and, hence, a smaller slope of the initial growth of $[O_2(a)]$ $(z > 15$ cm) (the mode with the additive $p_{O2} = 0.08$ Torr in Fig. 3). Note that the sources and drains of $O_2(a)$ associated with the excited atoms (reactions (8b) and (9)) were not significant for the $O_2(a)$ balance unlike the pronounced influence of the excited atoms on $O_2(b)$.

4. PRODUCTION/DEATH AND SPATIAL DISTRIBUTIONS OF $O_2(b)$ IN A FAST-FLOW GAS SYSTEM IN $O/O_2/N_2$ MIXTURES

Calculations using the 2D(r,z)-model with the same gas-phase (Table 1) and surface (s1)–(s3) processes of the five experimental modes corresponding to Fig. 6 from [20] with $[[O_2(b)]_{av}(z)$ profiles for different $O_2(X)$ additives also showed good agreement with $[O_2(b)]_{av}(z)$ measured along the tube.

As we can see from Fig. 6, these profiles realize different slopes of growth of the $[O_2(b)]_{av}(z)$ curves, their saturation, and even decline for $O_2(X)$ additives $p_{O2} \geqslant 0.05$ Torr. Note the incomplete description of the experimental parameters of these modes in [20] – the exact values of the gas pressure and the fraction of O atoms in the mixture are not given, typos in the concentrations of $O_2(X)$ additions in Table 1 in [20] (the concentrations 1.63×10^{14} and 3.26×10^{14} cm^{-3} should be increased by an order of magnitude), and ambiguity in using the introduced steady-state $[O_2(b)]_{ss}$ concentrations. The analysis of all experimental results given in that work allowed us to establish the parameters of the modes in Fig. 6 from [20] and use in the calculations the composition of the inlet 0.34%O/N_2 mixture and gas pressure $p_{gas} = 2.07$ Torr. The calculated $[O_2(b)]_{av}(z)$ profiles (Fig. 6) are established due to the balance of multiple $O_2(b)$ production and death reactions (Fig. 7). As for $O_2(a)$, there is considerable spatial heterogeneity in the rates of these reactions and the involvement (in addition to $O_2(h)$, O_2^{nt}, $O_2(a)$, and $O(^3P)$) of excited atoms as well as ozone and its vibrational states in both production and death of $O_2(b)$ (Fig. 7). We consider the roles of the principal reactions and the dependence of $[O_2(b)]$ $_{av}(z)$ concentration profiles on the gas pressure and the fraction of O atoms in the original mixture.

We begin our consideration with the simplest case without $O_2(X)$ additive. As we can see from the reaction rates (Fig. 7), in the unperturbed zone $z < 10$ cm, where there is no obvious influence of the $O_2(X)$ additive and the conditions are similar to the case without additive, the $O_2(b)$ production rate is determined by the balance of practically only two production reactions (3a), (9) and two death reactions (16), (18). Here, the rate of reaction (3a) is nearly constant along the tube and its

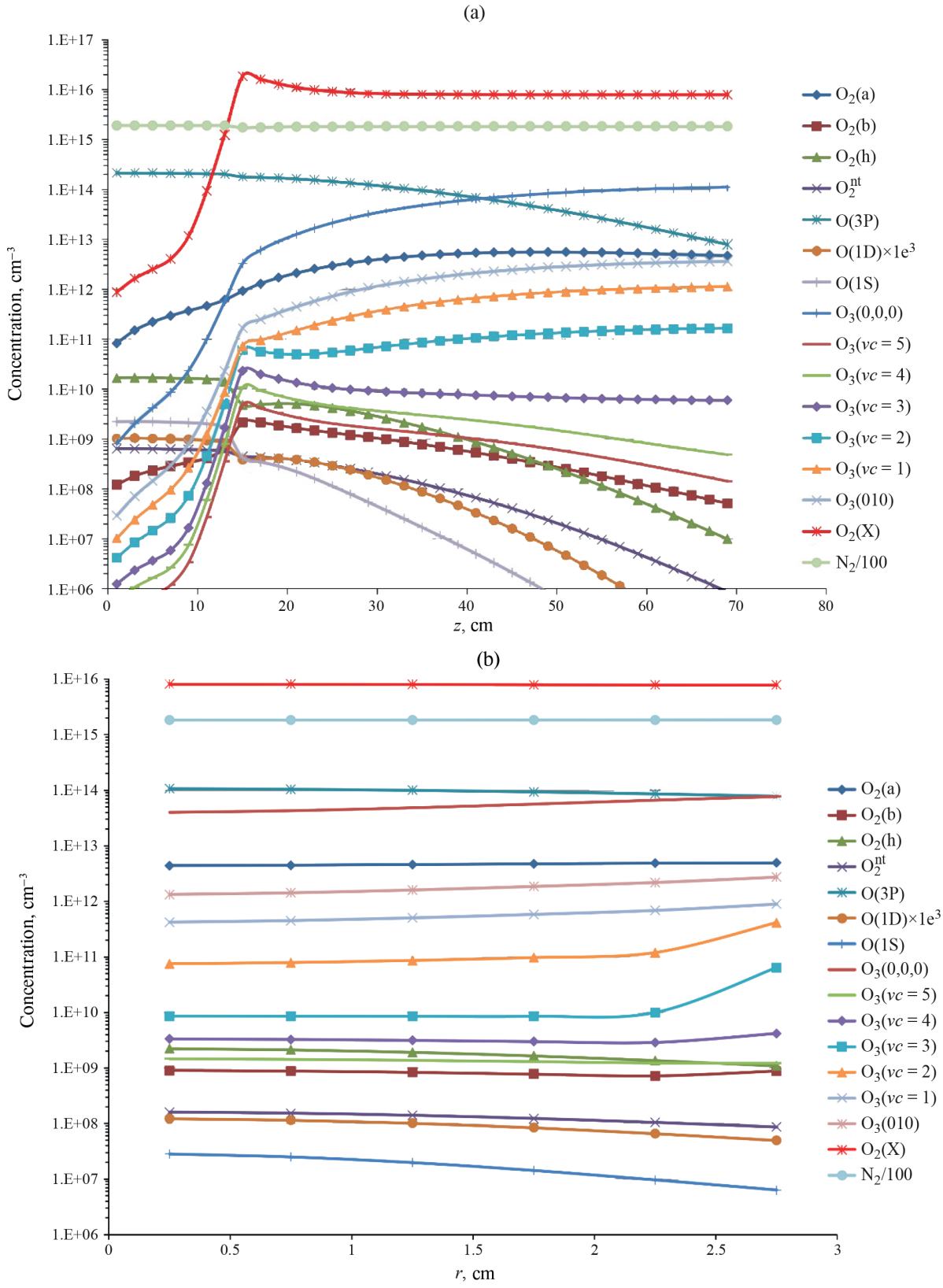

Fig. 5. Distributions of component concentrations (a) along the tube (along z for $r = 0.75$ cm) and (b) along the tube radius r for $z = 25$ cm for the mode with additive of 250 mTorr $O_2(X)$ to the inlet flow of the 0.11%O/N_2 mixture, the gas pressure in the tube is $p_{gas} = 6$ Torr. The concentration of the main gas N_2 is shown reduced by a factor of 100. The concentration of O(1d) is shown increased by a factor of 10^3.

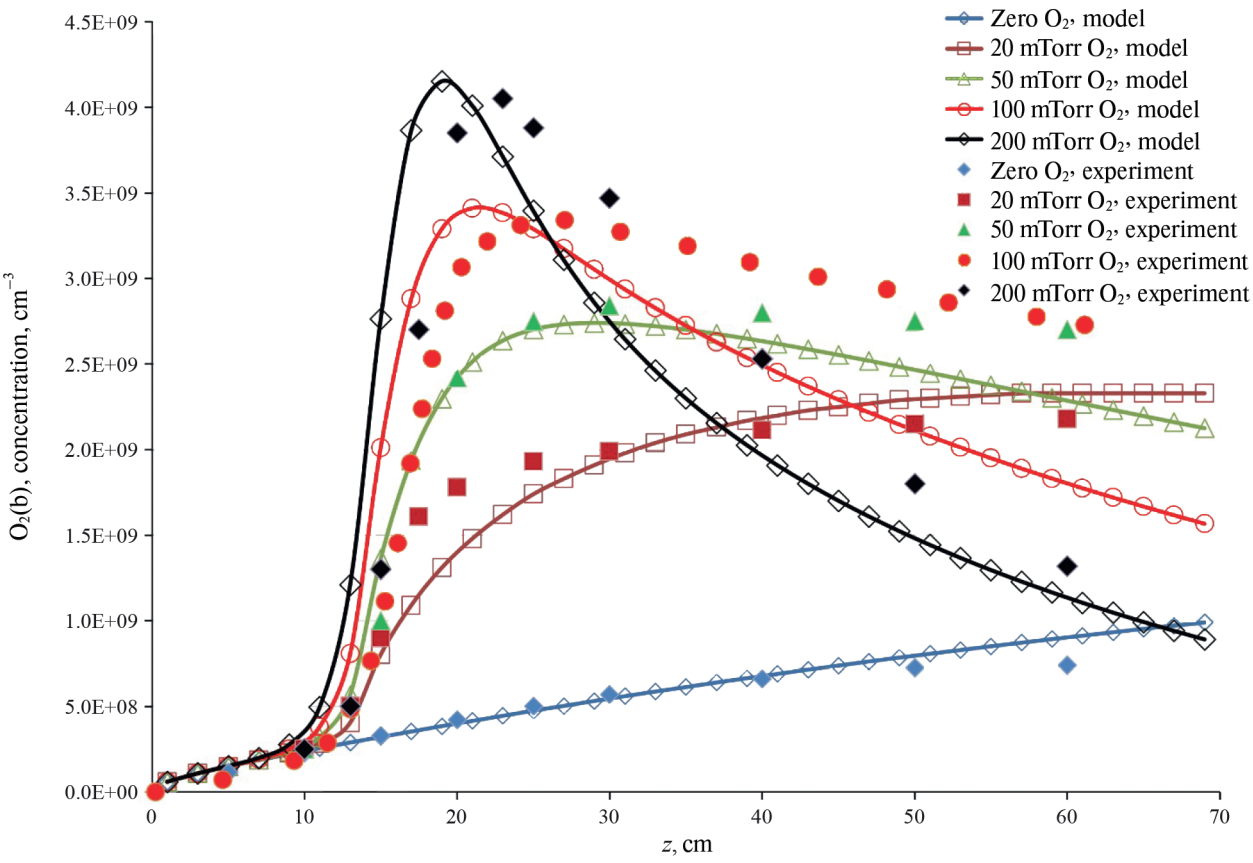

Fig. 6. Axial distributions of the $O_2(b)$ concentrations mean with respect to the tube diameter in the model and experiment [20] for different $O_2(X)$ additives (for z~15 cm) to the flow of the 0.34%O/N_2 mixture, the gas pressure in the tube is p_{gas} = 2.07 Torr.

contribution is comparable to that of reaction (9) only at the beginning of the tube at $z < 5$ cm. The rate of reaction (9) grows linearly by more than an order of magnitude along the tube (due to the respective increase in $O_2(a)$ concentration), which determines the increasing $[O_2(b)]_{av}(z)$ profile (Fig. 6) and the constant of reaction (9). The rate of principal reaction (9) increases drastically with the concentration of O atoms in the mixture (proportional to ~$[O]^4$) as a result of the dependencies of reactants $[O(^1S)]$~$[O]^2$ (due to the balance of reactions (2j) and (10)) and $[O_2(a)]$~$[O]^2$ (as shown in the previous section). This allows us to expect a high degree dependence $[O_2(b)]$~$[O]^m$ for $O_2(b)$ itself as well. Calculations for $[O] = 2.25 \times 10^{14}$ (Fig. 6) and 3.54×10^{14} cm^{-3} give local values of $[O_2(b)]_{av}(z = 25\ \text{cm})$ ~4.7×10^8 and 2.2×10^9 cm^{-3}, corresponding to m ~3.35. No experimental data for these dependences on [O] are given in [20]. A principal $O_2(b)$ source growing along the tube at the expense of $[O_2(a)](z)$ growth appears to be the only acceptable way to ensure $[O_2(b)]_{av}(z)$ growth without distorting the results in $O_2(X)$ additive modes. For instance, the alternative source $O_2(h) + O_2(X) \rightarrow O_2(b)$ + product with the required rate coefficient of ~2×10^{-13} cm^3/s resulted in a mismatch of an order of magnitude or more between the calculated and experimental $O_2(b)$ profiles in all modes considered with $O_2(X)$ additives. The same unacceptable results are obtained when introducing other, significantly increased as compared to Table 1, sources of $O_2(b)$, for instance, $O_2(h) + O_3 \rightarrow O_2(b)$ + products or $O_3 + O \rightarrow O_2(b) + O_2(X)$.

With the $O_2(X)$ additive introduced, the $O_2(b)$ concentration begins to be affected by many more reactions, including those involving ozone and $O_2(X)$ (Fig. 7), whose concentrations increase by several orders of magnitude (Fig. 8), as well as $O_2(h)$, $O_2(a)$, and $O(^1S)$. This makes it very difficult to analytically consider the complex balance of $O_2(b)$ production and death. Experimentally, it was found in [20] that the dependence of the additional growth of $[O_2(b)]_{av}$ on [O] (as compared to the case of zero $O_2(X)$ additive) just beyond the $O_2(X)$ injection zone is of first order ($m = 1$) for small additives, in particular for $[O_2(X)] = 4.48 \times 10^{14}$ cm^{-3} ($p_{O2} = 0.014$ Torr).

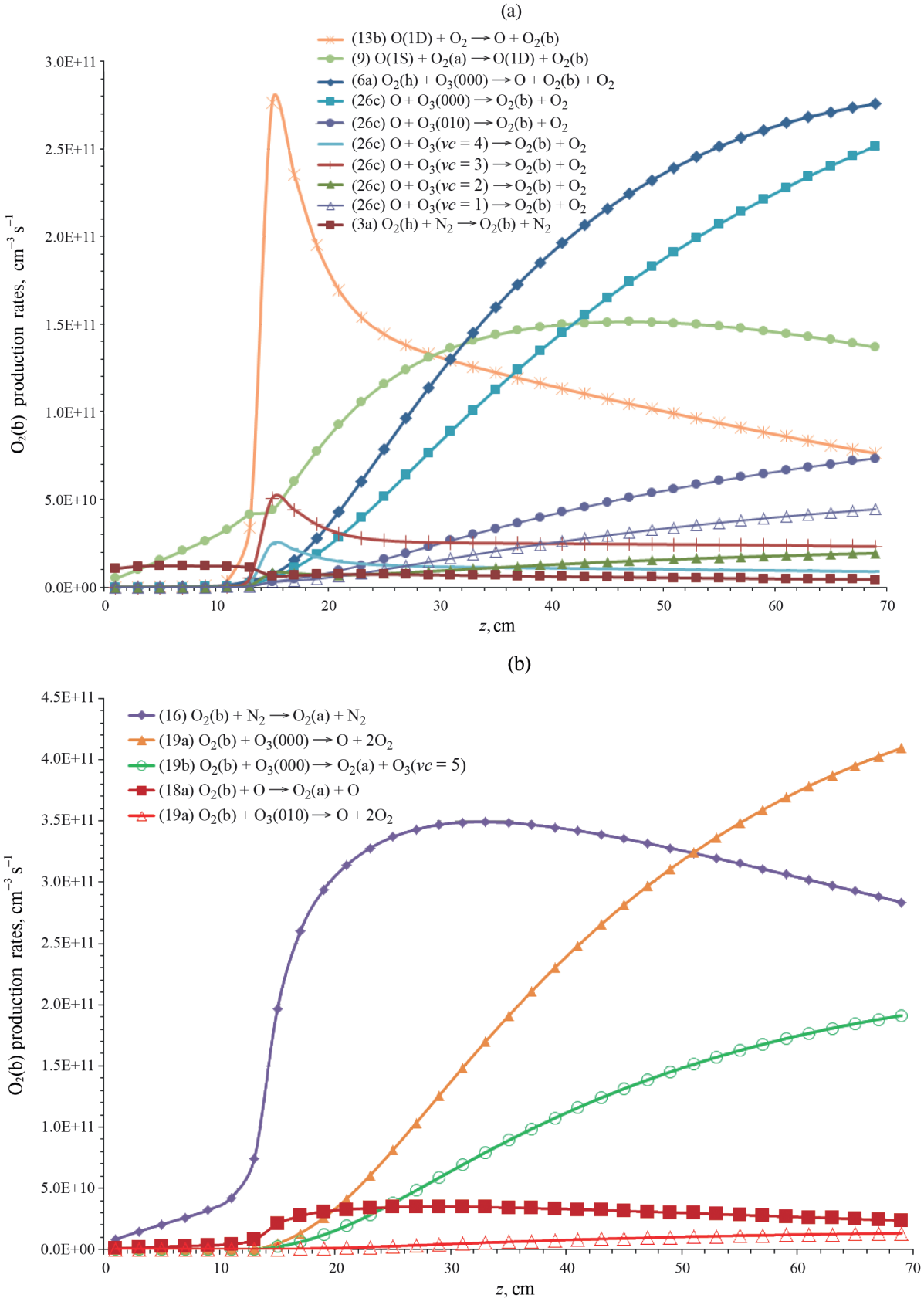

Fig. 7. Distributions (z,r = 0.75 cm) along the tube of production (a) and death (b) rates of O_2(b) for the mode with 0.05 Torr O_2(X) additive to the flow of the 0.34%O/N_2 mixture, the gas pressure in the tube is p_{gas} = 2.07 Torr.

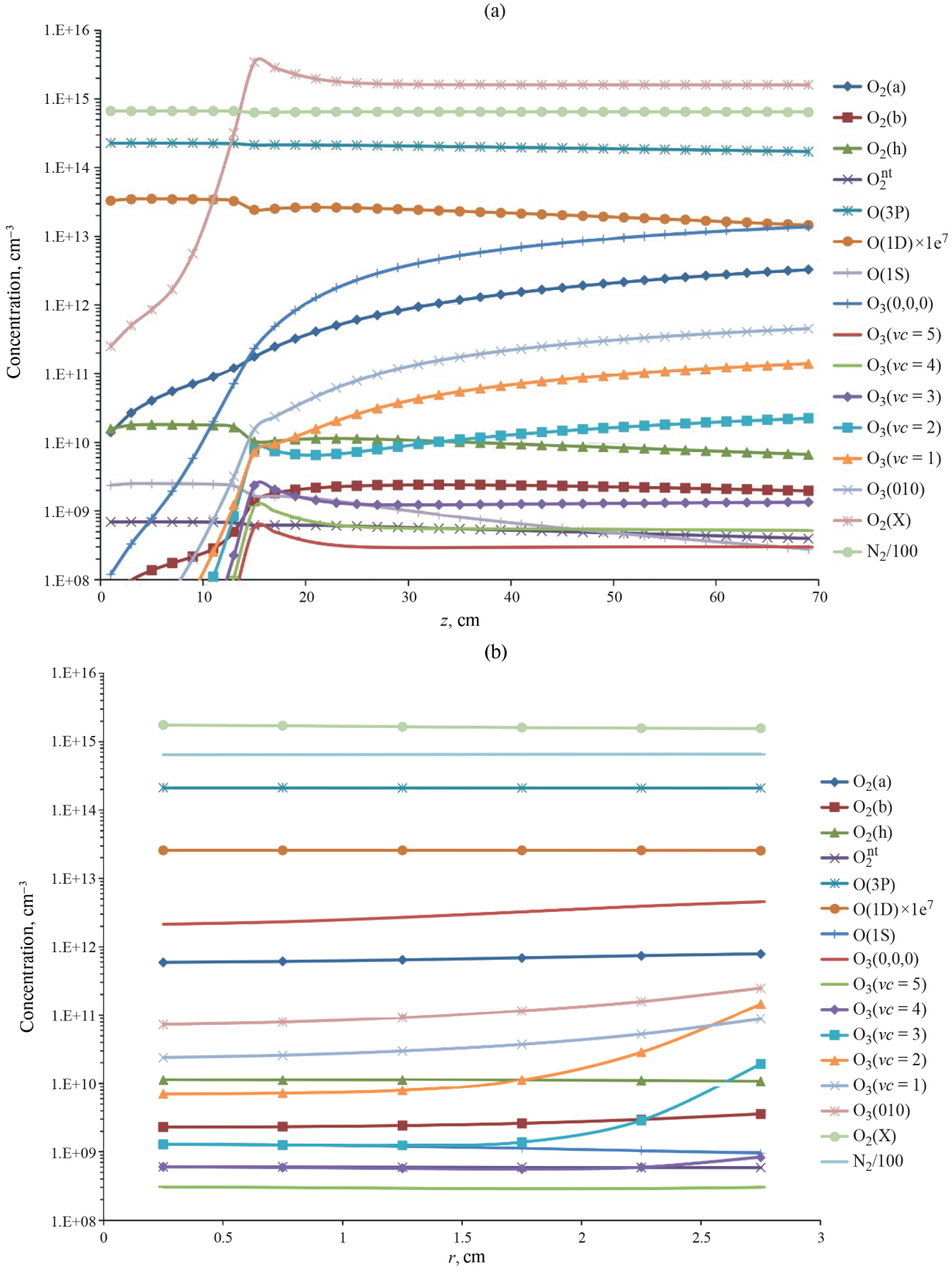

Fig. 8. Distributions of component concentrations (a) along the tube (with respect to z for $r = 0.75$ cm) and (b) along the tube radius r for $z = 25$ cm for the mode with 0.05 Torr $O_2(X)$ additive to the flow of the 0.34%O/N_2 mixture, the gas pressure in the tube is $p_{gas} = 2.07$ Torr. The concentration of the main gas N_2 is given with a scaling factor of 100. The O(1d) concentration is shown scaled up by a factor of 10^7.

By implication, this non-strictly defined value of additional $[O_2(b)]_{av}$ growth should be proportional to the gradient $d[O_2(b)]_{av}/dz$ in the narrow zone $z \sim 15–20$ cm of drastic $[O_2(b)]_{av}$ growth (Fig. 6). Additional calculations for $[O_2(X)] = 4.48 \times 10^{14}$ cm^{-3} and $p_{gas} = 2.07$ Torr showed that this gradient varies from 8×10^7 cm^{-4} for $[O] = 2.15 \times 10^{14}$ cm^{-3} to 2.3×10^8 cm^{-4} for $[O] = 3.54 \times 10^{14}$ cm^{-3}, which corresponds to the order $m = 2.1$ of the dependence on [O] different from the experimental $m = 1$.

However, for big additives, in particular, $p_{O2} \approx 0.2$ Torr, the experimental technique can be distorted by the unaccounted drop of $[O](z > 15$ cm) in the $O_2(b)$ measurement zone (as compared to the initial $[O](z = 0)$) and by the difficulty of comparing the measured $O_2(b)$ concentrations themselves in the zone of their drastic axial gradients (Fig. 6). The calculation for $[O] = 2.15 \times 10^{14}$ and 2.83×10^{14} cm^{-3} gives an order of $m = 1.3$ of the dependence of the gradient $d[O_2(b)]_{av}/dz$ on [O], while the experiment under these conditions yields $m = 2$ (Fig. 3 from [20]). However, the value 2.5×10^9 cm^{-3} of additional $[O_2(b)]_{av}$ growth in this figure for $[O] = 2.15 \times 10^{14}$ cm^{-3} contradicts the value of 3.2×10^9 cm^{-3} of additional growth in Fig. 2 from the same work [20] for almost the same conditions. For the latter value of the additional growth $[O_2(b)]_{av}$, the experimental dependence on [O] in Fig. 3 from [20] will have an order close to $m = 1$. Note that the complexity of the balance of multiple reactions of $O_2(b)$ production and death (Fig. 7) and drop of the $[O](z)$ concentration does not allow us to obtain accurate estimates in the analysis of dependences of $[O_2(b)]_{av}$ on the initial $[O](z = 0)$ concentration.

The analytical relations and the $O_2(b)$ balance discussed above lead to a weak dependence of $[O_2(b)]_{av}$ on the main gas pressure p_{N2} (on almost total pressure $p_{gas} \approx p_{N2}$). Calculations in the range $p = 2–6$ Torr confirm this. Thus, for $[O] = 2.15 \times 10^{14}$ cm^{-3} in the inlet flow and when p_{gas} was increased by a factor of three (from 2 to 6 Torr), the calculated maximum of $[O_2(b)]_{av}$ did not change for the case of zero $O_2(X)$ additive and dropped by ~50% for the additive $p_{O2} = 0.2$ Torr. No experimental data for the dependences on p_{O2} are given in [20].

As noted above, the $[O_2(b)]_{av}(z)$ axial profiles themselves that change dramatically with $O_2(X)$ added (Fig. 6) are determined by the complex of reactions illustrated in Fig. 7 for $p_{O2} = 0.05$ Torr. As we can see, the death of $O_2(b)$ is determined by quenching by N_2 and reactions with ozone. $O(^1D)$ quenching reactions on O_2 (13b) and $O(^1S)$ on $O_2(a)$ (9), as well as reactions involving ozone (including vibrationally excited ozone), are essential in $O_2(b)$ production. Assumed reaction (6a) is not critical yet allows for a 10% to 15% increase in the calculated $[O_2(b)]_{av}(z)$ in the downstream half of the tube for $p_{O2} = 0.02$ and 0.05 Torr, improving the correlation with the experimental profiles. For reactions of ozone with O atoms, the found fraction of ~1.7% of channel (26c) with the $O_2(b)$ product is sufficiently small and causes no contradiction with the results of red photolysis experiments [22]. Note also that an additional source of $O_2(b)$ sufficient to describe the experiments of [20] could be the reaction $O_2(h) + O_2(a) \rightarrow O_2(b) +$ product, but it would require a rate constant ~1.6×10^{-11} cm^3/s, which is rather high for such reactions. In [54], a rate constant of 8×10^{-11} cm^3/s was measured for the reaction of $O_2(A^3\Sigma_u^+)$ with $O_2(a)$ with unknown products.

Finally, we highlight that in this work, a rigid modeling scenario was purposely chosen assuming the same surface conditions in the two experimental works [19, 20], which used two types of passivating materials. Small differences in the surface block (s1) (s3) in the course of modeling these experiments allowed for a closer agreement between the calculated and experimental results to be achieved. However, such variation of ozone formation reactions on the surface is redundant against the background of the already achieved correlation of the principal trends and spatial profiles in different modes.

CONCLUSIONS

In this work, we performed two-dimensional 2D(r,z) modeling of the dynamics of recombining O/N_2 mixtures (with and without $O_2(X)$ additive) under the conditions of experiments [19, 20] in a fast-flow gas system, compared them with the experimental profiles of singlet oxygen $O_2(a)$ and $O_2(b)$, and established the main production and death reactions of $O_2(a)$ and $O_2(b)$. We proposed the interpretation of the reaction of the three-body recombination of O atoms on $M = N_2$, O_2 taking into account the reverse dissociation reaction of the resulting highly excited O_2^{nt} molecule and obtained he functional dependence of the resulting coefficient $k_{rec}(T)$ of the rate of three-body recombination of O atoms, which agrees well with the measured temperature dependences $k_{rec}(T)$. We proposed and analyzed the channels for further reaction and collision relaxation of O_2^{nt} and the resulting excited $O_2(h)$, $O_2(b)$, $O_2(a)$ molecules and $O(^1S)$, $O(^1D)$ atoms. We showed the importance of surface reactions of formation of vibrationally excited ozone $O_3(vc)$ (and death of O atoms) in the recombination of colliding $O_2(X)$ molecules with O atoms adsorbed on the surface, and subsequent reactions involving ozone in the production and death of $O_2(a)$ and $O_2(b)$. The developed reaction scheme allows us to describe

the experimental dependences of $[O_2(a)]_{av}(z)$ and $[O_2(b)]_{av}(z)$ on the pressure, the fraction of O in the initial O/N_2 mixture, and downstream $O_2(X)$ additives. We demonstrated the need to include the vibrational kinetics of ozone in the complete reaction scheme. We verified the rate coefficients of the processes $O + O_3(v) \rightarrow O_2(a) + O_2$ and $O + O_3(v) \rightarrow O_2(b) + O_2$, which are the sources of $O_2(a)$ and $O_2(b)$, respectively.

FUNDING

The study was supported by the Russian Science Foundation (grant no. 21-72-10040).

REFERENCES

1. *Kaufmann M., Gil-López S., López-Puertas M. et al.* // J. of Atmospheric and Solar-Terrestrial Physics. 2006. Vol. 68. No. 2. P. 202.
2. *Vlasov M., Klopovsky K., Lopaev D. et al.* // Cosmic Research. 1997. Vol. 35. No. 3. P. 219.
3. *Azyazov V.N., Heaven M.C.* // Intern. J. of Chemical Kinetics. 2014. Vol. 47. No. 2. P. 93.
4. *Torbin A.P., Mikheyev P.A., Pershin A.A. et al.* // "Molecular singlet delta oxygen quenching kinetics in the EOIL system" SPIE Proceedings 2015/02/03 2015.
5. *Lopaev D.V., Malykhin E.M., Zyryanov S.M.* // J. of Physics D: Applied Physics. 2010. Vol. 44. No. 1. P. 015202.
6. *Marinov D., Guerra V., Guaitella O. et al.* // Plasma Sources Science and Technology. 2013. Vol. 22. No. 5. P. 055018.
7. *Ellerweg D., von Keudell A., Benedikt J.* // Plasma Sources Science and Technology. 2012. Vol. 21. No. 3. P. 034019.
8. *Klopovskii K., Kovalev A., Lopaev D. et al.* // J. of Experimental and Theoretical Physics – J EXP THEOR PHYS. 1995. Vol. 80. P. 603.
9. *Klopovskii K., Popov N., Proshina O. et al.* // Plasma Physics Reports. 1997. Vol. 23. P. 165.
10. *Kogelschatz U.* // Plasma Chemistry and Plasma Processing. 2003. Vol. 23. No. 1. P. 1.
11. *Samoilovich V.G., Gibalov V.I., Kozlov K.V.* Physical chemistry of barrier discharge. Moscow: Moscow University Publishing House, 1989.
12. *Mikheyev P.A., Demyanov A.V., Kochetov I.V. et al.* // Plasma Sources Science and Technology. 2020. Vol. 29. No. 1. P. 015012.
13. *Zosimov A.V., Lunin V.V., Samoilovich V.G. et al.* // Russ. J. Phys. Chem. 2016. Vol. 90. No. 8. P. 1687.
14. *Mankelevich Yu.A., Poroykov A.Yu., Rakhimova T.V. et al.* // Russ. J. Phys. Chem. 2016. Vol. 90. No. 9. P. 1896.
15. *Mankelevich Yu.A., Voronina E.N., Poroykov A.Yu. et al.* // Plasma Phys. Rep. 2016. Vol. 42. No. 10. P. 956.
16. *Torbin A.P., Pershin A.A., Azyazov V.N.* // Physics and Electronics. Izv. Samara Scientific Center of RAS. 2014. Vol. 16. No. 4. P. 17.
17. *Pershin A.A., Torbin A.P., Haven M. et al.* // Short communications on physics of the P.N. Lebedev Physical Institute of the Russian Academy of Sciences. 2015. Vol. 12. P. 74.
18. *Azyazov V.N., Mikheyev P., Postell D. et al.* // Chemical Physics Letters. 2009. Vol. 482. No. 1–3. P. 56–61.
19. *Ali A.A., Ogryzlo E.A., Shen Y.Q. et al.* // Canadian J. of Physics. 1986. Vol. 64. No. 12. P. 1614.
20. *Ogryzlo E.A., Shen Y.Q., Wassell P.T.* // Journal of Photochemistry. 1984. Vol. 25. No. 2–4. P. 389.
21. *Yankovsky V.* // Advances in Space Research. 2021. Vol. 67. No. 3. P. 921.
22. *Lunin V.V., Popovich M.P., Tkachenko S.N.* Physical chemistry of ozone. Moscow: Moscow University Publishing House, 1998.
23. *Mankelevich Yu.A., Rakhimova T.V., Voloshin D.G. et al.* // Russ. J. Phys. Chem. 2023. Vol. 97. No. 5. P. 1033.
24. *Booth J.P., Chatterjee A., Guaitella O. et al.* // Plasma Sources Sci. Technol. 2022. Vol. 31. No. 6. P. 065012.
25. *Mankelevich Y.A., Rakhimov A.T., Suetin N.V.* // Diamond and Related Materials. 1995. Vol. 4. No. 8. P. 1065.
26. *Mankelevich Y.A., Ashfold M.N.R., Ma J.* // J. of Applied Physics. 2008. Vol. 104. No. 11. P. 113304.
27. *Braginskiy O.V., Vasilieva A.N., Klopovskiy K.S. et al.* // J. of Physics D: Applied Physics. 2005. Vol. 38. No. 19. P. 3609.
28. *Booth J.P., Guaitella O., Zhang S. et al.* // Plasma Sources Science and Technology. 2023. Vol. 32. No. 9. P. 095016.
29. *Campbell I.M., Thrush B.A.* // Proceedings of the Royal Society of London. Series A. Mathematical and Physical Sciences. 1967. Vol. 296. No. 1445. P. 222.
30. *Slanger T.G., Copeland R.A.* // Chemical Reviews. 2003. Vol. 103. No. 12. P. 4731.
31. *Esposito F., Armenise I., Capitta G. et al.* // Chemical Physics. 2008. Vol. 351. No. 1–3. P. 91.
32. *Manion J. A., Huie R. E., Levin R. D. et al.* // NIST Chemical Kinetics Database, NIST Standard Reference Database 17, Version 7.0 (Web Version), Release 1.6.8, Data version 2015.09: National Institute of Standards and Technology, Gaithersburg, Maryland, 20899-8320 2015.
33. *Campbell I.M., Gray C.N.* // Chemical Physics Letters. 1973. Vol. 18. No. 4. P. 607.
34. *Pejaković D.A., Kalogerakis K.S., Copeland R.A. et al.* // J. of Geophysical Research: Space Physics. 2008. Vol. 113. No. A4. P. A04303.

35. *Huestis D.L.* // Atmospheres in the Solar System: Comparative Aeronomy. 2002. P. 245.
36. *Zagidullin M.V., Khvatov N.A., Medvedkov I.A. et al.* // J. of Phys.Chem.A. 2017. Vol. 121. No. 39. P. 7343.
37. *Wayne R.P.* //Singlet Molecular Oxygen Advances in Photochemistry. Wiley. 1969. P. 311.
38. *Stott I.P., Thrush B.A.* // Proceedings of the Royal Society of London. A. Mathematical and Physical Sciences. 1989. Vol. 424. No. 1866. P. 1.
39. *Vasiljeva A.N., Klopovskiy K.S., Kovalev A.S. et al.* // J. of Physics D: Applied Physics. 2004. Vol. 37. No. 17. P. 2455.
40. *McEwan M. J., Phillips L. F.* Chemistry of the atmosphere. London: Arnold. 1975.
41. *Atkinson R., Welge K.H.* // J. of Chemical Physics. 1972. Vol. 57. No. 9. P. 3689.
42. *Slanger T.G., Black G.* // J. of Chem. Physics. 1976. Vol. 64. No. 9. P. 3763.
43. *London G., Gilpin R., Schiff H.I. et al.* // J. of Chem. Physics. 1971. Vol. 54. No. 10. P. 4512.
44. *Dunlea E.J., Ravishankara A.* // Physical Chemistry Chemical Physics. 2004. Vol. 6. No. 9. P. 2152.
45. *Capitelli M., Ferreira C.M., Gordiets B.F. et al.* // Plasma Kinetics in Atmospheric Gases Springer Series on Atomic, Optical, and Plasma Physics: Springer Berlin Heidelberg 2000.
46. *Yee J.H., Guberman S.L., Dalgarno A.* // Planetary and Space Science. 1990. Vol. 38. No. 5. P. 647.
47. *Slanger T.G., Black G.* // The J. of Chemical Physics. 1979. Vol. 70. No. 7. P. 3434.
48. *Hoskinson A.R., Rawlins W.T., Galbally-Kinney K.L. et al.* // J. of Physics D: Applied physics. 2022. Vol. 55. No. 12. P. 125208.
49. *Clark I.D., Wayne R.P.* // Chemical Physics Letters. 1969. Vol. 3. No. 6. P. 405.
50. *Baulch D.L., Cox R.A., Crutzen P.J. et al.* // J. of Physical and Chemical Reference Data. 1982. Vol. 11. No. 2. P. 327.
51. *Morin J., Bedjanian Y., Romanias M.N.* // Intern. J. of Chemical Kinetics. 2016. Vol. 49. No. 1. P. 53.
52. *Shefov N.N., Semenov A.I., Khomich V.Yu.* Radiation of the upper atmosphere as an indicator of its structure and dynamics. Moscow: GEOS, 2006.
53. *Kirillov A.S.* // Chemical Physics Letters. 2014. Vol. 592. P. 103.
54. *Kenner R.D., Ogryzlo E.A.* // Canadian J. of Physics. 1984. Vol. 62. No. 12. P. 1599.